doi.org/10.26434/chemrxiv.7687358.v1

Fused Hybrid Linkers for Metal–Organic Frameworks-Derived Bifunctional Oxygen Electrocatalysts

Kefeng Ping, Alan Braschinsky, Mahboob Alam, Rohit Bhadoria, Valdek Mikli, Arvo Mere, Jaan Aruväli, Sergei Vlassov, Mati Kook, Mihkel Rähn, Väino Sammelselg, Kaido Tammeveski, Nadezda Kongi, Pavel Starkov

Submitted date: 07/02/2019 • Posted date: 07/02/2019

Citation information: Ping, Kefeng; Braschinsky, Alan; Alam, Mahboob; Bhadoria, Rohit; Mikli, Valdek; Mere, Arvo; et al. (2019): Fused Hybrid Linkers for Metal–Organic Frameworks-Derived Bifunctional Oxygen Electrocatalysts. ChemRxiv. Preprint.

Preparation of electrocatalysts often relies on the use of multiple starting materials – inorganic salts or organometallic precursors, nanostructured carbon supports, organic additives, dopants and carbonization under modifying atmospheres (e.g. NH_3 or H_2) – with the examples of electrocatalysts arising from a single precursor being much less common. Herein, we have surveyed a series of heterobivalent scaffolds to identify an iron/benzimidazole-based metal– organic framework as a uniform starting material. By merging the catechol and imidazole units together, we get direct entry into a highly efficient bifunctional oxygen electrocatalyst, which alleviates the need for additional dopants and modifying conditions (ORR: E_{on} = 1.01 V, $E_{1/2}$ = 0.87 V vs. RHE in 0.1 M KOH; OER: 1.60 V @10 mA cm^{-2} in 0.1 M KOH; ΔE = 0.73 V). We demonstrate that by fine-tuning the chemical nature of an organic linker, one is able modulate the electrochemical properties of a single precursor-derived electrocatalyst material.

File list (2)

Fused Hybrid Linkers for Metal–Organic Frameworks-Derived Bifunctional Oxygen Electrocatalysts

Kefeng Ping,[a] Alan Braschinsky,[b] Mahboob Alam,[a] Rohit Bhadoria,[a] Valdek Mikli,[c] Arvo Mere,[c] Jaan Aruväli,[d] Sergei Vlassov,[e] Mati Kook,[e] Mihkel Rähn,[e] Väino Sammelselg,[b,e] Kaido Tammeveski,[b] Nadežda Kongi,[b,*] and Pavel Starkov[a,*]

[a] *Department of Chemistry & Biotechnology, Tallinn University of Technology, 12618 Tallinn, Estonia*

[b] *Institute of Chemistry, University of Tartu, 50411 Tartu, Estonia*

[c] *Department of Materials & Environmental Technology, Tallinn University of Technology, 19086 Tallinn, Estonia*

[d] *Institute of Ecology and Earth Sciences, University of Tartu, 50411 Tartu, Estonia*

[e] *Institute of Physics, University of Tartu, 50411 Tartu, Estonia*

E-mail: nadezda.kongi@ut.ee; pavel.starkov@taltech.ee

Abstract

Preparation of electrocatalysts often relies on the use of multiple starting materials – inorganic salts or organometallic precursors, nanostructured carbon supports, organic additives, dopants and carbonization under modifying atmospheres (e.g. NH_3 or H_2) – with the examples of electrocatalysts arising from a single precursor being much less common. Herein, we have surveyed a series of heterobivalent scaffolds to identify an iron/benzimidazole-based metal–organic framework as a uniform starting material. By merging the catechol and imidazole units together, we get direct entry into a highly efficient bifunctional oxygen electrocatalyst, which alleviates the need for additional dopants and modifying conditions (ORR: E_{on} = 1.01 V, $E_{1/2}$ = 0.87 V *vs.* RHE in 0.1 M KOH; OER: 1.60 V @10 mA cm^{-2} in 0.1 M KOH; ΔE = 0.73 V). We demonstrate that by fine-tuning the chemical nature of an organic linker, one is able modulate the electrochemical properties of a single precursor-derived electrocatalyst material.

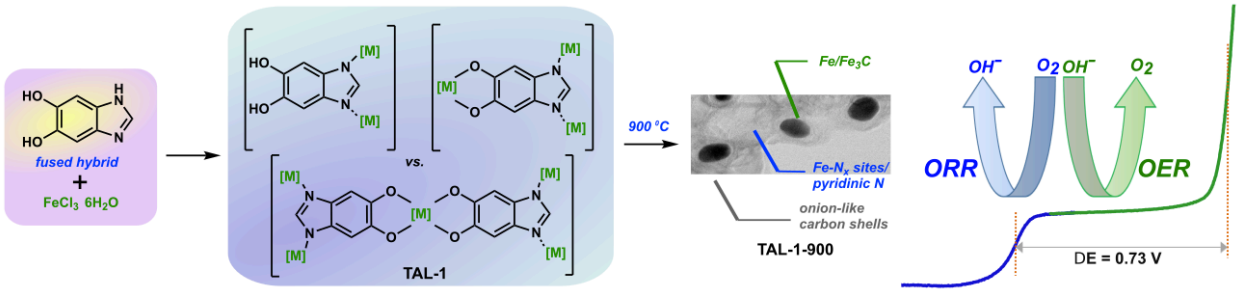

Main Text

Metal–organic frameworks (MOFs) are a great platform for designing and building novel materials with a foray into applications in energy storage and conversion, e.g. water splitting, fuel cells and metal–air batteries.[1,2] MOFs incorporate both the metal centres and organic ligands, which serve as essential building blocks.[3] Hence, having an intrinsic ability to modify their combinations may lead to more efficient, modular electrocatalyst materials. The oxygen reduction reaction (ORR) electrocatalysts have been exemplary with different MOFs having been traditionally employed as carbon-scaffolds and nitrogen-rich sources.[2] However, they often necessitate using dopants to raise the overall performance of the underlying electrocatalyst.[2] To date, only a few MOF-derived materials were shown to serve as highly efficient electrocatalysts

for ORR (Figure 1). Among them are iron-based MIL-88B-NH_2,[4] cobalt-based ZIF-67,[5] and bimetallic systems based on MET-6[6] and hexaaminebenzene.[7]

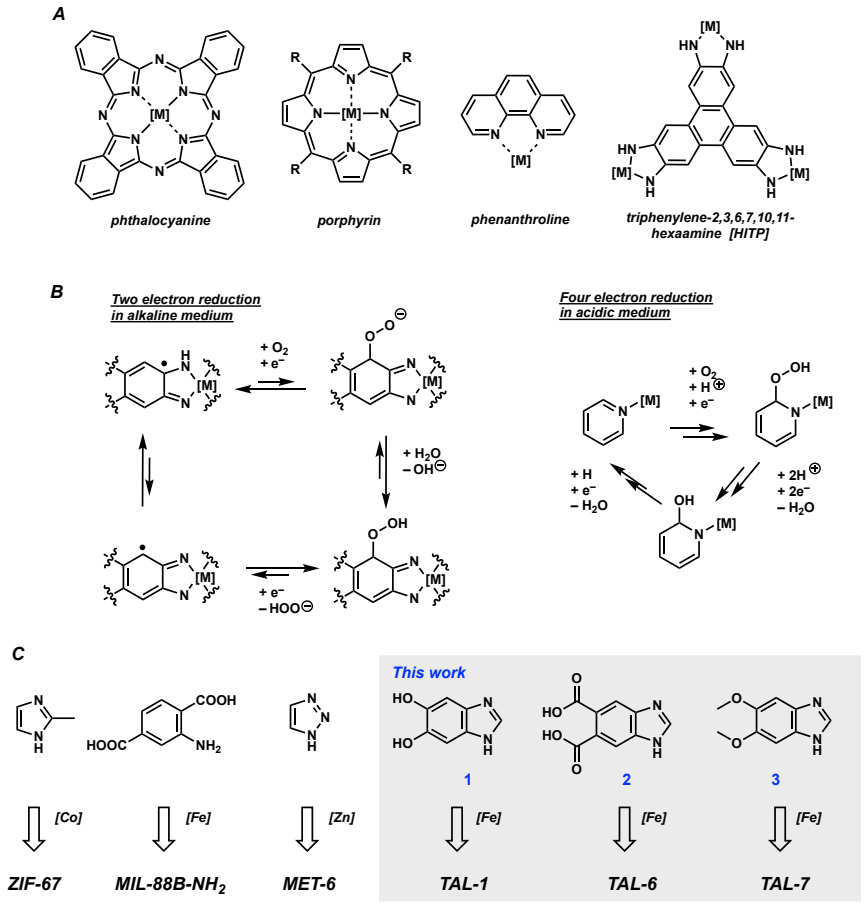

Fig. 1 a) Organic ligands complexed to a metal (M), widely used to prepare M–N–C cathode electrocatalyst materials for ORR. b) Non-innocent ligand participation in the ORR.[8,9] c) Metal–organic frameworks used as single precursors for unsupported and non-doped ORR electrocatalysts.

In the ORR domain, the use of organic constituents for fabrication of earth-abundant metals-based electrocatalyst materials (M–N–C) dates back[10] to the report of the first M–N–C catalyst, cobalt phthalocyanine (Figure 1a).[11] Since then, a number of complementary metal complexes (e.g. phthalocyanines,[11,12] porphyrins,[13–16] phenanthrolines,[17–19] and ferrocene[20]) have been examined. Recent work indicated that conductive MOFs such as $M_3(HITP)_2$[8,21] and $M_3(HHTP)_2$[21b,22] may also serve as potential ORR catalysts. While such systems show low intrinsic activity, they have been used to demonstrate that organic constituents can participate in the electrochemical O_2 reduction through complementary ligand-centric mechanisms (Figure 1b).[8]

Herein, we introduce a new family of carbon-rich[23] benzimidazole-based MOF precursors, which are equipped with additional functional groups to modulate their electronic and ligating properties (Figure 1c). We assess them as ORR and oxygen evolution reaction (OER)[24] catalyst materials to identify that monocatechol/imidazole fused hybrid **1** is the best performing ligand for fabricating effective bifunctional oxygen (ORR/OER, ΔE = 0.73 V in 0.1 M KOH) electrocatalyst from an iron MOF-derived single-component precursor.

We envisaged building Fe–N–C catalyst from a single MOF precursor by using designer ligands. While one would typically rely on multidirectional, symmetric structures based on porphyrins, phthalocyanines and hexa-substituted triphenylenes, we wished to focus on constructing several related heterobivalent units. This gave us means to see whether and how

different organic ligands can affect the morphology and catalytic performance of the final electrocatalyst materials. To test this hypothesis, we prepared three MOFs as insoluble, polycrystalline powders TAL-1, TAL-6 and TAL-7 from iron chloride and 5,6-disubstituted-1*H*-benzo*[d]*imidazoles (**1**, R = OH; **2**, R = COOH; **3**, R = OCH_3) as ligands. For TAL-1, we have tested various ratios of metal to linker (2:1, 1:1, 1:2), however, they did not significantly alter the chemical composition of the material obtained (Table S2). TAL materials were then subjected to carbonization at T = 900 °C and acid leaching to give three electrocatalysts termed TAL-1-900, TAL-6-900 and TAL-7-900, respectively.

The structure and morphology of prepared electrocatalysts was examined by powder X-ray diffraction (PXRD), X-ray photoelectron spectroscopy (XPS), high-resolution scanning and transmission electron microscopy (HRSEM and HRTEM) (Figure 2 and SI). The HRTEM images of TAL-1-900 and TAL-7-900 show dense Fe/Fe_3C nanocrystals, which are embedded into the structured, onion-like shells of carbon (Figure 2d). The characteristic layer distance of the iron/iron carbide particles was 0.203 nm and the spacing of the carbon shells was 0.371 nm, and they remain constant after acid leaching.[25] The presence of α-Fe/Fe_3C in TAL-1-900 and TAL-7-900 was confirmed by PXRD (Figure 2b). TAL-6-900 material, however, incorporated iron oxide nanoparticles with a characteristic interplanar spacing of 0.29 nm corresponding to d (220) of Fe_3O_4.[26] The XPS survey spectra show the presence of carbon, oxygen, nitrogen and iron on the surface of the catalyst materials (Figures 2c and S1 and Table S1). The deconvolved N1s region shows the presence of Fe–N_x and pyridinic nitrogen species, which are both required for high ORR/OER activity.[10,24]

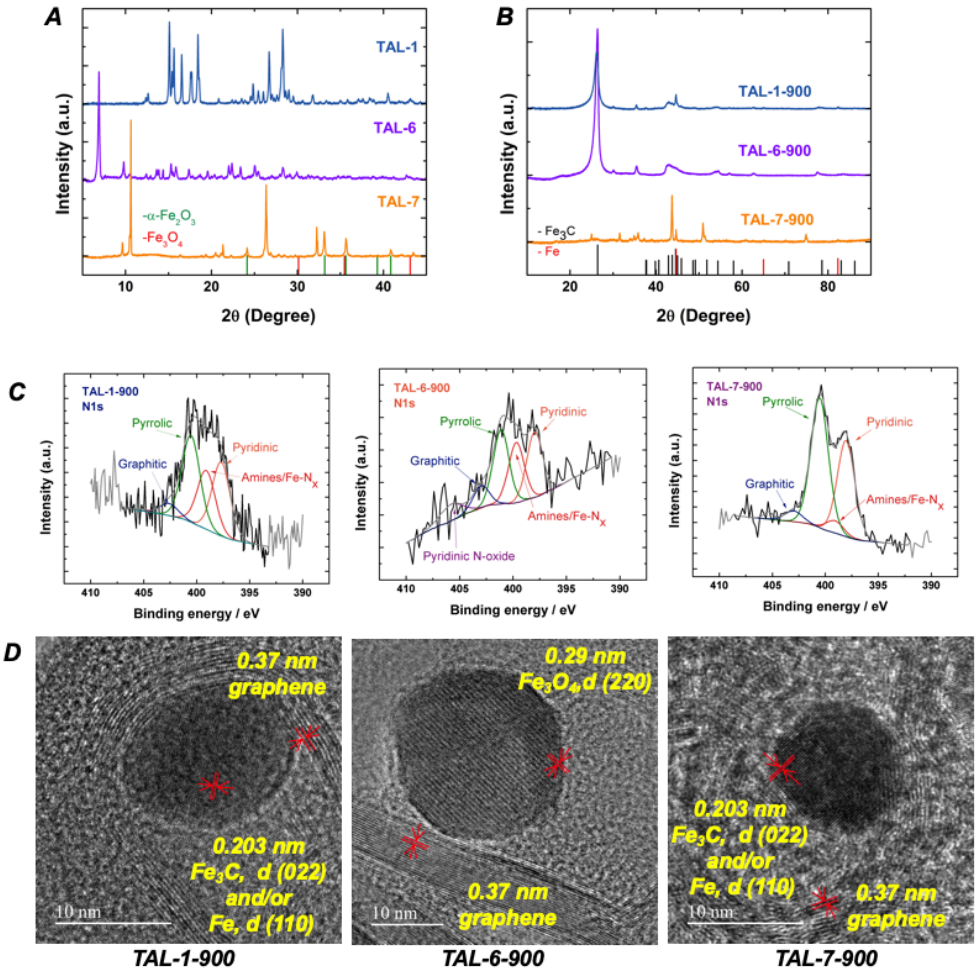

Fig. 2 Physical and morphological characterization of TAL-derived composites and precursors. a) PXRD patterns of TAL precursors, b) PXRD patterns of TAL-derived catalyst materials. c) XPS core-level spectra in the N1s region. d) HRTEM micrographs. Scale bars, 10 nm.

With optimized materials in hand, we evaluated electrochemical behaviour of TAL-1-900, TAL-6-900 and TAL-7-900 using cyclic voltammetry (CV) in argon-saturated 0.1 M KOH solution at room temperature (Figure 3a). We compared electrochemical performance against the state-of-the-art commercial 20 wt% Pt/C catalyst (E-TEK; loading 20 μg_{Pt} cm^{-2}). The TAL electrocatalysts exhibited a symmetrical and rectangular CV profile without any characteristic redox features. The double-layer capacitance was larger than that of Pt/C, indicating that TAL-derived materials have high electrochemically active surface area.

The rotating disk electrode (RDE) technique was employed to study the ORR kinetics of TAL-modified glassy carbon (GC) electrodes in O_2-saturated 0.1 M KOH (Figure 3b). TAL-1-900 (R = OH) performed on par with 20 wt% Pt/C catalyst (E_{on} = 1.01 V, $E_{1/2}$ = 0.87 V vs. E_{on} = 1.01 V, $E_{1/2}$ = 0.85 V). While TAL-6-900 was less active than TAL-1-900, electrocatalyst TAL-7-900 showed good performance, albeit with a slight offset in the onset potential (E_{on}). Notably, when **1** and iron(III) chloride were pre-mixed in DMF for 2 h, concentrated and subjected to carbonization, the afforded material was not effective in the ORR tests (data not shown). Hence, the formation of corresponding MOFs is a prerequisite for fabrication of an active electrocatalyst.

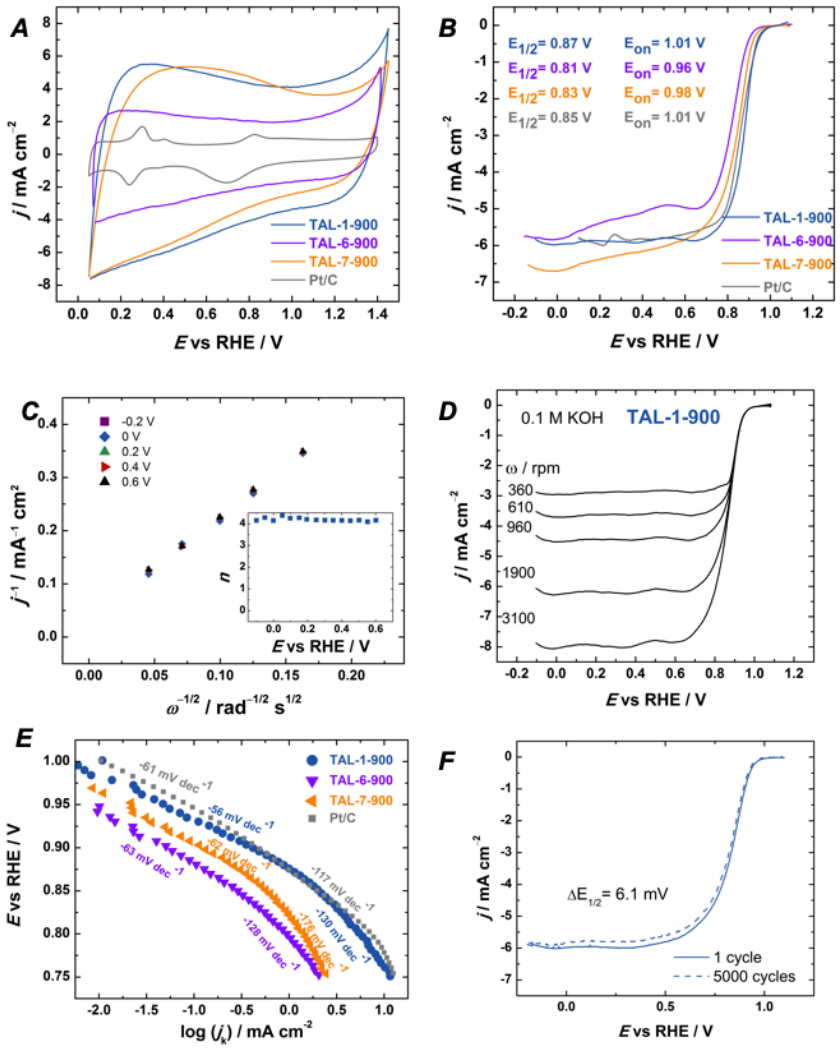

Fig. 3 Electrochemical oxygen reduction on TAL materials in 0.1 M KOH. a) Cyclic voltammograms of electrocatalyst-modified GC electrodes (under argon); v = 50 mV s^{-1}. b) RDE polarization curves for TAL and Pt/C modified GC electrodes at 1900 rpm; v = 10 mV s^{-1}. c) Koutecky–Levich plots for O_2 reduction on TAL-1-900 modified GC electrode, inset: number of electrons transferred per O_2 molecule. d) RDE polarization data on oxygen reduction recorded at various rotation rates on TAL-1-900 modified GC electrode; v = 10 mV s^{-1}. e) Tafel plots for O_2 reduction on TAL and Pt/C catalysts. f) Electrochemical stability test for TAL-1-900.

Koutecky−Levich (K–L) plots (Figure 3c) were constructed from the RDE data (Figure 3d) and showed good linearity and parallelism for TAL-1-900. This behaviour is typical for the first-order reaction kinetics with respect to the concentration of dissolved dioxygen. The number of electrons transferred per O_2 molecule (n) was calculated from the RDE data using the K–L equation.[27] All TAL-derived electrocatalysts follow the desired four-electron transfer pathway (n = 4; the insets in Figures 3d and S5), indicating that oxygen is reduced fully to water. Kinetic current densities were calculated using the K–L equation at 0.9 V and compared. TAL-1-900 exhibited the j_k value similar to that of Pt/C (2.0 vs 1.9 mA cm^{-2}).

In the kinetically controlled region of the ORR, the Tafel plots of TAL-1-900 overlapped with those of Pt/C, with two distinct regions present at different potential ranges (Figure 3e). TAL-1-900 catalyst had similar dual Tafel slopes in the low and high overpotential regions as Pt/C (–56 and –130 mV dec^{-1} *vs.* –61 and –117 mV dec^{-1}). The Tafel slope value of –56 mV dec^{-1} for TAL-1-900 indicates that the rate determining step in the ORR is the formation of adsorbed intermediates (OOH).

After continuous cycling from 0.6 to 1.0 V vs. RHE, electrocatalytic activity of TAL-1-900 remained at the same level without any change in the onset potential (Figure 3f). However, only a slight decrease in diffusion-limited current density was observed indicating that its porosity remains largely unaffected.

As TAL-1-900 showed excellent electrocatalytic behaviour in the ORR tests, we wished to see how it performs in oxygen evolution reaction (Figure 4). The materials with high bifunctional activity are used in metal–air batteries,[24] however, the active sites responsible for OER's high activity are different from the sites required for ORR.[10,24] To assess the overall oxygen electrode activity (ΔE) of TAL electrocatalysts, the potential differences of OER at a current density of 10 mA cm^{-2} and of ORR at a current density of –3 mA cm^{-2} were calculated at electrode rotation rate of 1600 rpm. The bifunctional ORR/OER activity of TAL-1-900 (ΔE = 0.73 V; E_{10} = 1.60 V @10 mA cm^{-2}) is among the best reported to date (Table S3), while TAL-6-900 and TAL-7-900 were less active (ΔE = 0.83 and 0.78 V, respectively).

TAL-1-900 has a Tafel slope of 84 mV dec^{-1} (Figure 4b), which is considerably smaller than those of TAL-6-900 (95 mV dec^{-1}), TAL-7-900 (112 mV dec^{-1}) and Pt/C (112 mV dec^{-1}), indicating faster OER kinetics. The durability of TAL-1-900 catalyst was evaluated by chronoamperometry test at applied potential of 1.6 V (Figure 4c). The current density of TAL-1-900 catalyst shows slight increase during the testing time, demonstrating that the catalyst exhibits excellent durability towards OER. Electrocatalytic OER behaviour also remained unchanged after continuous cycling of TAL-1-900 electrode 5000 times in the potential range between 1.0 and 1.8 V vs. RHE (Figure 4d).

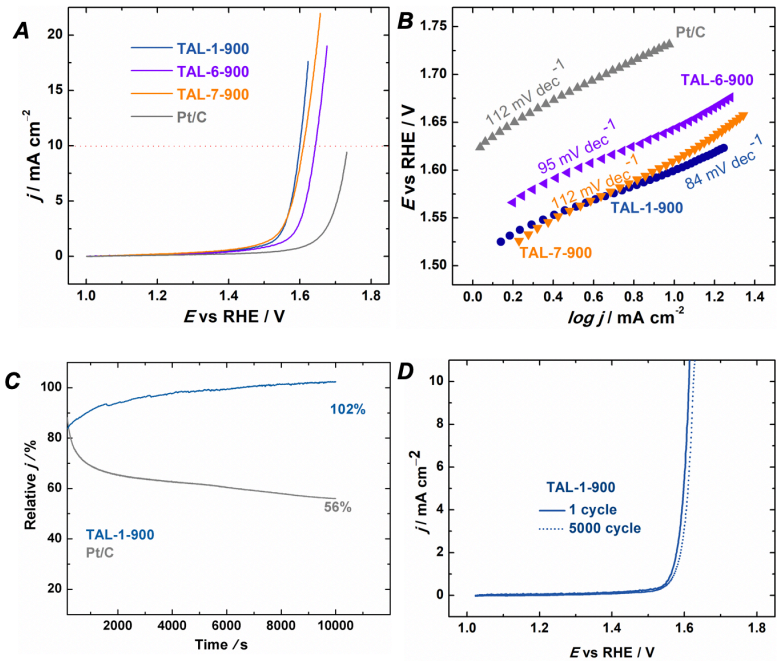

Fig. 4 Electrochemical oxygen evolution on TAL materials in 0.1 M KOH. a) LSV curves for TAL-modified GC electrodes, $v = 10$ mV s^{-1}. b) Tafel plots based on LSV curves. c) Chronoamperometric response for TAL-1-900 and Pt/C recorded at applied potential of 1.6 V. d) Electrochemical stability of TAL-1-900 after 5000 cycles.

The overall relationship TAL-1-900 > TAL-7-900 >> TAL-6-900 indicates that electron-rich precursors may boost the ORR/OER catalyst's activity. Our observation, however, may have several alternative explanations. These include rendering the activity of Fe–N_x sites and pyridinic nitrogen;[9,10] initiation of ligand-centred 2*e*×2*e* pathway similar to the one proposed for HITP and HHTP ligands (Figure 1b);[8,21,22] creation of hypothetical mixed Fe–N_x/O_y sites; the control of pore sizes and other structural aspects of the carbonised molecular meshwork. Notably, in the case of TAL-6-900, we observed formation of Fe_3O_4 but not Fe/Fe_3C nanocrystals. While the M–N_x species are known to reduce dioxygen in the ORR via a direct reduction of oxygen to hydroxide (a *4e* process), the less active metal-based particles (e.g. Fe/Fe_3C,[25] Fe_2N[25e]) do it in a stepwise 2*e*×2*e* manner (first, forming the peroxides and then decomposing them to water).[10,25] This observation also suggests that the organic linker itself may modulate not only the rate of formation of nanocrystals embedded into carbon support but also their composition.

Interestingly, we observe an improvement in TAL-1-900 vs. TAL-7-900 performance. This may be attributed to the catechol unit itself because the iron–catechol complexation is sufficiently strong[28] and several polycatechol-based covalent[29] and metal–organic frameworks were previously reported.[22,30] Hence, employing catechol precursors may lead to increased conductivity of the final material and/or additional (electro)chemical contributions (e.g. enhanced carbonisation or ligand-centred *2e*×*2e* processes).

In summary, we have surveyed a series of carbon-rich, fused hybrid-type organic linkers to construct iron-based MOFs, which serve as direct precursors for efficient bifunctional (ORR/OER) electrocatalyst materials. This single-precursor strategy relied on carbonisation of benzimidazole derivatives under non-modifying (N_2) atmosphere. The active Fe–N–C materials contained Fe–N_x sites, pyridinic nitrogen and Fe/Fe_3C nanocrystals, except for TAL-6-900, which contained Fe_3O_4 and was much less active. Our results confirm that there is a direct link between the electronic and ligating properties of the initial organic ligand and the electrocatalytic properties of the final electrocatalysts. Translating this into practice will require further exploration of structure–activity relationships of chemically decorated carbon-rich precursors.

Conflict of interest

P.S., K.P., K.T. and N.K. are inventors on a related patent application owned by TalTech and the University of Tartu.

Acknowledgements

This research was supported by Estonian Research Council Grant PUT1290 and TalTech Young Investigator Grant B62 (both to P.S.); Institutional Research Funding IUT20–16 of the Estonian Ministry for Education and Research and the Centre of Excellence TK141: Advanced materials and high-technology devices for energy recuperation systems from the EU ERDF program (both to K.T.); and Estonian Research Council Grant PSG250 (to N.K.). We thank COST Action CA15135 MuTaLig members for helpful discussions. TalTech (V.M.) and UT HRSEM (S.V.) facilities are supported by TK141 (TAR16016), IUT–T4 and PUT1689, respectively. TalTech (A.M.) and UT (J.A.) XRD facilities are supported by IUT19–4 and TK141. UT HRTEM (M.R., V.S.) facilities are supported by Institutional Research Funding IUT2–24 of the Estonian Ministry for Education and Research. K.P. acknowledges the Estonian Smart Specialization PhD Fellowship.

References

[1] (a) Seh, Z. W.; Kibsgaard, J.; Dickens, C. F.; Chorkendorff, I.; Nørskov, J. K.; Jaramillo, T. F. Combining theory and experiment in electrocatalysis: Insights into materials design. *Science* **2017,** *355,* eaad4998. DOI:10.1126/science.aad4998
(b) Katsounaros, I.; Cherevko, S.; Zeradjanin, A. R.; Mayrhofer, K. J. J. Oxygen electrochemistry as a cornerstone for sustainable energy conversion. *Angew. Chem. Int. Ed.* **2014,** *53,* 102–121. DOI:10.1002/anie.201306588

[2] (a) Liao, P.-Q.; Shen, J.-Q.; Zhang, J.-P. Metal–organic frameworks for electrocatalysis. *Coord. Chem. Rev.* **2018,** *373,* 22–48. DOI:10.1016/j.ccr.2017.09.001
(b) Wu, H, B, Lou, X. W. Metal-organic frameworks and their derived materials for electrochemical energy storage and conversion: Promises and challenges. *Sci. Adv.* **2017,** *3,* eaap9252. DOI:10.1126/sciadv.aap9252

[3] (a) Diercks, C. S.; Kalmutzki, M. J.; Diercks, D. J.; Yaghi, O. M. Conceptual advances from Werner complexes to metal–organic frameworks. *ACS Cent. Sci.* **2018,** 4,1457–1464. DOI:10.1021/acscentsci.8b00677
(b) Kalmutzki, M. J.; Hanikel, N.; Yaghi, O. M. Secondary building units as the turning point in the development of the reticular chemistry of MOFs. *Sci. Adv.* **2018,** *4,* eaat9180. DOI:10.1126/sciadv.aat9180

[4] Zhao, S.; Yin, H.; Du, L.; He, L.; Zhao, K.; Chang, L.; Yin, G.; Zhao, H.; Liu, S.; Tang, Z. Carbonized nanoscale metal–organic frameworks as high performance electrocatalyst for oxygen reduction reaction. *ACS Nano* **2014,** *8,* 12660–12668. DOI:10.1021/nn505582e

[5] Xia, B. Y.; Yan, Y.; Li, N.; Wu, H. B.; Loi, X. W.; Wang, X. A metal–organic framework-derived bifunctional oxygen electrocatalyst. *Nat. Energy* **2016,** *1,* 15006. DOI:10.1038/nenergy.2015.6

[6] Zhao, R.; Liang, Z.; Gao, S.; Yang, C.; Zhu, B.; Zhao, J.; Qu, C.; Zou, R.; Xu, Q. Puffing up energetic metal–organic frameworks to large carbon networks with hierarchical porosity and atomically dispersed metal sites. *Angew. Chem. Int. Ed.* **2019,** *58,* 1975–1979. DOI:10.1002/anie.201811126

[7] Shinde, S. S.; Lee, C. H.; Jung, J.-Y.; Wagh, N. K.; Kim, S.-H.; Kim, D.-H.; Lin, C.; Lee, S. U.; Lee, J. H. Unveiling dual-linkage 3D hexaiminobenzene metal–organic frameworks towards long-lasting advanced reversible Zn–air batteries. *Energy Environ. Sci.* **2019,** *12,* ASAP. DOI:10.1039/c8ee02679c

[8] Miner, E. M.; Gul, S.; Ricke, N. D.; Pastor, E.; Yano, J.; Yachandra, V. K.; van Voorhis, T.; Dincă, M. Mechanistic evidence for ligand-centered electrocatalytic oxygen reduction with the conductive

MOF Ni_3(hexaiminotriphenylene)$_2$. *ACS Catal.* **2017,** *7,* 7726–7731. DOI:10.1021/acscatal.7b02647

[9] (a) Guo, D.; Shibuya, R.; Akiba, C.; Saji, S.; Kondo, T.; Nakamura, J. Active sites of nitrogen-doped carbon materials for oxygen reduction reaction clarified using model catalysts. *Science* **2016,** *351,* 361–365. DOI:10.1126/science.aad0832
(b) Kabir, S.; Artyushkova, K.; Serov, A.; Atanassov, P. Role of Nitrogen moieties in N-doped 3D-graphene nanosheets for oxygen electroreduction in acidic and alkaline media. *ACS Appl. Mater. Interfaces* **2018,** *10,* 11623–11632. DOI:10.1021/acsami.7b18651

[10] (a) Xia, W.; Mahmood, A.; Liang, L.; Zou, R.; Guo, S. Earth-abundant nanomaterials for oxygen reduction. *Angew. Chem. Int. Ed.* **2016,** *55,* 2650–2676. DOI:10.1002/anie.201504830
(b) Masa, J.; Xia, W.; Muhler, M.; Schuhmann, W. On the role of metals in nitrogen-doped carbon electrocatalysts for oxygen reduction. *Angew. Chem. Int. Ed.* **2015,** *54,* 10102–10120. DOI:10.1002/anie.201500569
(c) Ge, X.; Sumboja, A.; Wuu, D.; An, T.; Li, B.; Goh, F. W. T.; Hor, T. S. A.; Zong, Y.; Liu, Z. Oxygen reduction in alkaline media: from mechanisms to recent advances of catalysts. *ACS Catal.* **2015,** *5,* 4643–4667. DOI:10.1021/acscatal.5b00524
(d) Sarapuu, A.; Kibena-Põldsepp, E.; Borghei, M.; Tammeveski, K. Electrocatalysis of oxygen reduction on heteroatom-doped nanocarbons and transition metal–nitrogen–carbon catalysts for alkaline membrane fuel cells. *J. Mater. Chem. A* **2018,** *6,* 776–804. DOI:10.1039/c7ta08690c
(e) Shao, M.; Chang, Q.; Dodelet, J.-P.; Chenitz, R. Recent advances in electrocatalysts for oxygen reduction reaction. *Chem. Rev.* **2016,** *116,* 3594–3657. DOI:10.1021/acs.chemrev.5b00462

[11] Jasinski, R. A new fuel cell cathode catalyst. *Nature* **1964,** *201,* 1212–1213. DOI:10.1038/2011212a0

[12] Jiang, R.; Li, L.; Sheng, T.; Hu, G.; Chen, Y.; Wang, L. Edge-site engineering of atomically dispersed Fe–N_4 by selective C–N bond cleavage for enhanced oxygen reduction reaction activities. *J. Am. Chem. Soc.* **2018,** *140,* 11594–11598. DOI:10.1021/jacs.8b07294

[13] Zhang, W.; Lai, W.; Cao, R. Energy-related small molecule activation reactions: Oxygen reduction and hydrogen and oxygen evolution reactions catalyzed by porphyrin- and corrole-based systems. *Chem. Rev.* **2017,** *117,* 3717–3797. DOI:10.1021/acs.chemrev.6b00299

[14] Sa, Y. J.; Seo, D.-J.; Woo, J.; Lim, J.-T.; Cheon, J. Y.; Yang, S. Y.; Lee, J. M.; Kang, D.; Shin, T. J.; Shin, H. S.; Jeong, H. Y.; Kim, C. S.; Kim, M. G.; Kim, T.-Y.; Joo, S. H. A general approach to preferential formation of active Fe–N_x sites in Fe–N/C electrocatalysts for efficient oxygen reduction reaction. *J. Am. Chem. Soc.* **2016,** *138,* 15046–15056. DOI:10.1021/jacs.6b09470

[15] Jahan, M.; Bao, Q.; Loh, K. P. Electrocatalytically active graphene–porphyrin MOF composite for oxygen reduction reaction. *J. Am. Chem. Soc.* **2012,** *134,* 6707–6713. DOI:10.1021/ja211433h

[16] Xiang, Z.; Xue, Y.; Cao, D.; Huang, L.; Chen, J.-F.; Dai, L. Highly efficient electrocatalysts for oxygen reduction based on 2D covalent organic polymers complexed with non-precious metals. *Angew. Chem. Int. Ed.* **2014,** *53,* 2433–2437. DOI:10.1002/anie.201308896

[17] Lefèvre, M.; Proietti, E.; Jaouen, F.; Dodelet, J.-P. Iron-based catalysts with improved oxygen reduction activity in polymer electrolyte fuel cells. *Science* **2009,** *324,* 71–74. DOI:10.1126/science.1170051

[18] Strickland, K.; Miner, E.; Jia, Q.; Tylus, U.; Ramaswamy, N.; Liang, W.; Sougrati, M.; Jaouen, F.; Mukerjee, S. Highly active oxygen reduction non-platinum group metal electrocatalyst without direct metal-nitrogen coordination. *Nat. Commun.* **2015,** *6,* 7343. DOI:10.1038/ncomms8343

[19] Ratso, S.; Ranjbar Sahraie, N.; Sougrati, M. T.; Käärik, M.; Kook, M.; Saar, R.; Paiste, P.; Jia, Q.; Leis, J.; Mukerjee, S.; Jaouen, F.; Tammeveski, K. Synthesis of highly-active Fe–N–C catalysts for

PEMFC with carbide-derived carbons. *J. Mater. Chem. A* **2018,** *6,* 14663–14674. DOI:10.1039/c8ta02325e

[20] Hu, Y.; Jensen, J. O.; Zhang, W.; Cleemann, L. N.; Xing, W.; Bjerrum, N. J.; Li, Q. Hollow spheres of iron carbide nanoparticles encased in graphitic layers as oxygen reduction catalysts. *Angew. Chem. Int. Ed.* **2014,** *53,* 3675–3679. DOI:10.1002/anie.201400358

[21] (a) Miner, E. M.; Fukushima, T.; Sheberla, D.; Sun, L.; Surendranath, Y.; Dincă, M. Electrochemical oxygen reduction catalysed by Ni_3(hexaiminotriphenylene)$_2$. *Nat. Commun.* ***2016,*** *7,* 10942. DOI:10.1038/ncomms10942
(b) Miner, E. M.; Wang, L.; Dincă, M. Modular O_2 electroreduction activity in triphenylene-based metal–organic frameworks. *Chem. Sci.* **2018,** *9,* 6289–6291. DOI:10.1039/c8sc02049c

[22] Liu, X.-H.; Hu, W.-L.; Jiang, W.-J.; Yang, Y.-W.; Niu, S.; Sun, B.; Wu, J.; Hu, J.-S. Well-defined metal–O_6 in metal–catecholates as a novel active site for oxygen electroreduction. *ACS Appl. Mater. Interfaces* **2017,** *9,* 28473−28477. DOI:10.1021/acsami.7b07410

[23] Kong, D.; Gao, Y.; Xiao, Z.; Xu, X.; Li, X.; Zhi, L. Rational design of carbon-rich materials for energy storage and conversion. *Adv. Mater.* **2018,** ASAP, DOI:10.1002/adma.201804973

[24] (a) Huang, Z.-F.; Wang, J.; Peng, Y.; Jung, C.-Y.; Fisher, A.; Wang, X. Design of efficient bifunctional oxygen reduction/evolution electrocatalyst: recent advances and perspectives. *Adv. Energy Mater.* **2017,** *7,* 1700544. DOI:10.1002/aenm.201700544
(b) Jiao, Y.; Zheng, Y.; Jaroniec, M.; Qiao, S. Z. Design of electrocatalysts for oxygen- and hydrogen-involving energy conversion reactions. *Chem. Soc. Rev.* **2015,** *44,* 2060–2086. DOI:10.1039/c4cs00470a

[25] (a) Jiang, W. J.; Gu, L.; Li, L.; Zhang, Y.; Zhang, X.; Zhang, L. J.; Wang, J. Q.; Hu, J. S.; Wei, Z.; Wan, L. J. Understanding the high activity of Fe–N–C electrocatalysts in oxygen reduction: Fe/Fe_3C nanoparticles boost the activity of Fe–N_x. *J. Am. Chem. Soc.* **2016,** *138,* 3570–3578. DOI:10.1021/jacs.6b00757
(b) Bhattacharyya, S.; Konkena, B.; Jayaramulu, K.; Schuhmann, W.; Maji, T. K. Synthesis of nano-porous carbon and nitrogen doped carbon dots from an anionic MOF: a trace cobalt metal residue in carbon dots promotes electrocatalytic ORR activity. *J. Mater. Chem. A* **2017,** *5,* 13573–13580. DOI:10.1039/c7ta00281e
(c) Varnell, J. A.; Tse, E. C. M.; Schulz, C. E.; Fister, T. T.; Haasch, R. T.; Timoshenko, J.; Frenkel, A. I.; Gewirth, A. A. Identification of carbon-encapsulated iron nanoparticles as active species in non-precious metal oxygen reduction catalysts. *Nat. Commun.* **2016,** *7,* 12582. DOI:10.1038/ncomms12582
(d) Kim, J. H.; Sa, Y. J.; Jeong, H. Y.; Joo, S. H. Roles of Fe−N_x and Fe−Fe_3C@C species in Fe−N/C electrocatalysts for oxygen reduction reaction. *ACS Appl. Mater. Interfaces* **2017,** *9,* 9567–9575. DOI:10.1021/acsami.6b13417
(e) Sun, T.; Jiang, Y.; Wu, Q.; Du, L.; Zhang, Z.; Yang, L.; Wang, X.; Hu, Z. Is iron nitride or carbide highly active for oxygen reduction reaction in acidic medium? *Catal. Sci. Technol.* **2017,** *7,* 51–55. DOI:10.1039/c6cy01921h

[26] Yang, S.; Jiang, J.-T.; Xu, C.-Y.; Wang, Y.; Xu, Y.-Y.; Cao, L.; Zhen, L. Synthesis of Zn(II)-doped magnetite leaf-like nanorings for efficient electromagnetic wave absorption. *Sci. Rep.* **2017,** *7,* 45480. DOI:10.1038/srep45480

[27] Bard, A. J.; Faulkner, L. R. *Electrochemical Methods: Fundamentals and Applications;* Wiley, **2001.**

[28] Filippidi, E; Cristiani, T. R.; Eisenbach, C. D.; Waite, J. H.; Israelachvili, J. N.; Ahn, B. K.; Valentine, M. T. Toughening elastomers using mussel-inspired iron-catechol complexes. *Science* ***2017,*** *358,* 502–505. DOI:10.1126/science.aao0350

[29] (a) Côté, A. P.; Benin, A. I.; Ockwig, N. W.; O'Keeffe, M.; Matzger, A. J.; Yaghi, O. M. Porous, crystalline, covalent organic frameworks. *Science* **2005,** *310,* 1166–1170. DOI:10.1126/science.1120411

(b) Spitler, E. L.; Dichtel, W. R. Lewis acid-catalysed formation of two-dimensional phthalocyanine covalent organic frameworks. *Nat. Chem.* **2010,** *2,* 672–677. DOI:10.1038/nchem.695

[30] (a) Hmadeh, M.; Lu, Z.; Liu, Z.; Gándara, F.; Furukawa, H.; Wan, S.; Augustyn, V.; Chang, R.; Liao, L.; Zhou, F.; Perre, E.; Ozolins, V.; Suenaga, K.; Duan, X.; Dunn, B.; Yamamto, Y.; Terasaki, O.; Yaghi, O. M. New porous crystals of extended metal-catecholates. *Chem. Mater.* **2012,** *24,* 3511–3513. DOI:10.1021/cm301194a
(b) Nguyen, N. T.; Furukawa, H.; Gándara, F.; Trickett, C. A.; Jeong, H. M.; Cordova, K. E.; Yaghi, O. M. Three-dimensional metal-catecholate frameworks and their ultrahigh proton conductivity. *J. Am. Chem. Soc.* **2015,** *137,* 15394–15397. DOI:10.1021/jacs.5b10999
(c) Park, J.; Hinckley, A. C.; Huang, Z.; Feng, D.; Yakovenko, A. A.; Lee, M.; Chen, S.; Zou, X.; Bao, Z. Synthetic routes for a 2D semiconductive copper hexahydroxybenzene metal–organic framework. *J. Am. Chem. Soc.* **2018,** *140,* 14533–14537. DOI:10.1021/jacs.8b06666

Supplementary Information

for

Fused hybrid linkers for metal–organic framework-derived bifunctional oxygen electrocatalysts

Kefeng Ping,[a] Alan Braschinsky,[b] Mahboob Alam,[a] Rohit Bhadoria,[a] Valdek Mikli,[c] Arvo Mere,[c] Jaan Aruväli,[d] Sergei Vlassov,[e] Mati Kook,[e] Mihkel Rähn,[e] Väino Sammelselg,[b,e] Kaido Tammeveski,[b] Nadežda Kongi,[b,*] and Pavel Starkov[a,*]

[a] *Department of Chemistry & Biotechnology, Tallinn University of Technology, 12618 Tallinn, Estonia*

[b] *Institute of Chemistry, University of Tartu, 50411 Tartu, Estonia*

[c] *Department of Materials & Environmental Technology, Tallinn University of Technology, 19086 Tallinn, Estonia*

[d] *Institute of Ecology and Earth Sciences, University of Tartu, 50411 Tartu, Estonia*

[e] *Institute of Physics, University of Tartu, 50411 Tartu, Estonia*

*****Corresponding authors. E-mail: nadezda.kongi@ut.ee; pavel.starkov@taltech.ee

Table of Contents

1 Additional Data

Figure S1. The XPS survey spectra and Fe2p core-level XPS spectra for TAL-X-900 materials

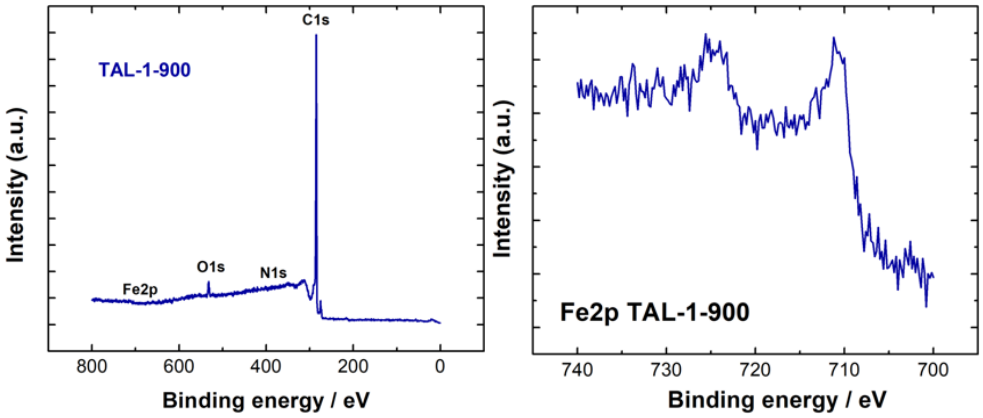

TAL-1-900

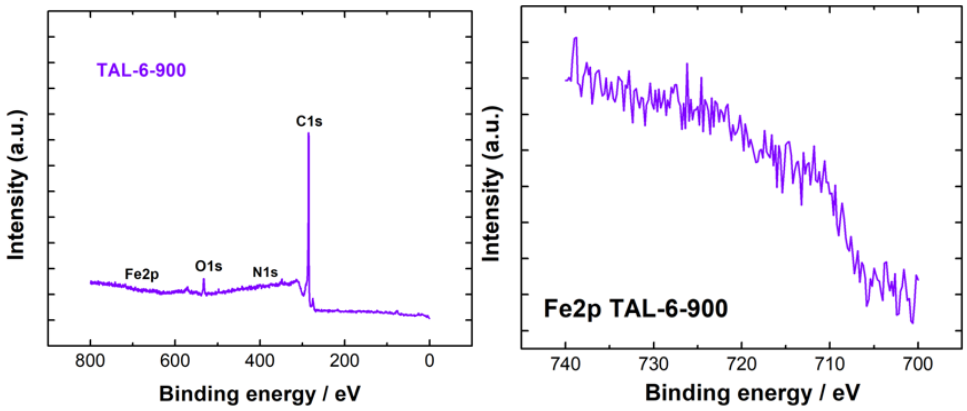

TAL-6-900

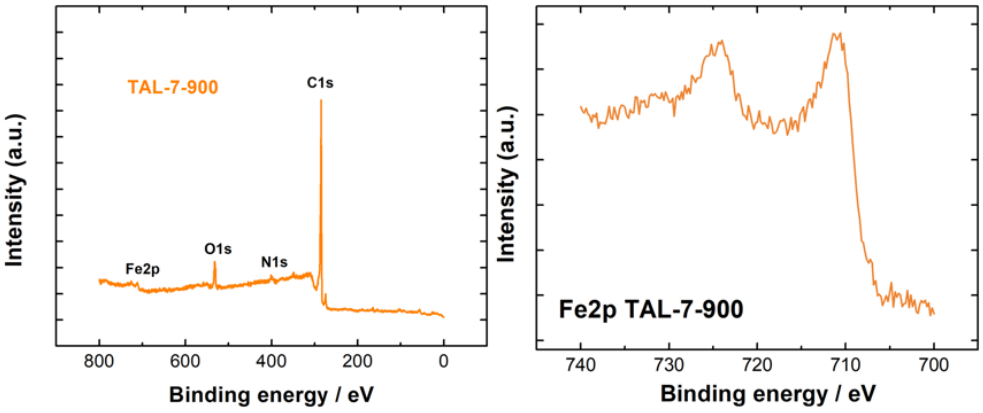

TAL-7-900

Table S1. Contents of different nitrogen and carbon moieties found *on the surface* of the catalyst material, relative to the total nitrogen and carbon content in TAL-X-900 materials.

	Total N content at%	*N–O %*	*Graphitic %*	*Pyrrolic %*	*Fe–N_x %*	*Pyridinic %*
TAL-1-900	0.6	0	5	37	25	32
TAL-6-900	0.4	10	9	30	24	27
TAL-7-900	1.0	1	4	51	5	38

	Total C content at%	*C–O–C, C–OH %*	*C=O %*	*O–C=O %*	*Carbide %*	*π-π* %*	*sp^2 %*	*sp^3 %*
TAL-1-900	97.1	6	1	0	7	9	66	11
TAL-6-900	97.4	2	3	2	7	6	63	17
TAL-7-900	93.5	8	3	2	6	7	42	34

Table S2. Elemental analysis of TAL-1 prepared from different metal/ligand ratios

starting M/L	*Carbon %*	*Hydrogen %*	*Nitrogen %*
2:1	33.54	3.23	13.50
1:1	36.31	3.18	14.16
1:2	39.65	3.05	15.03

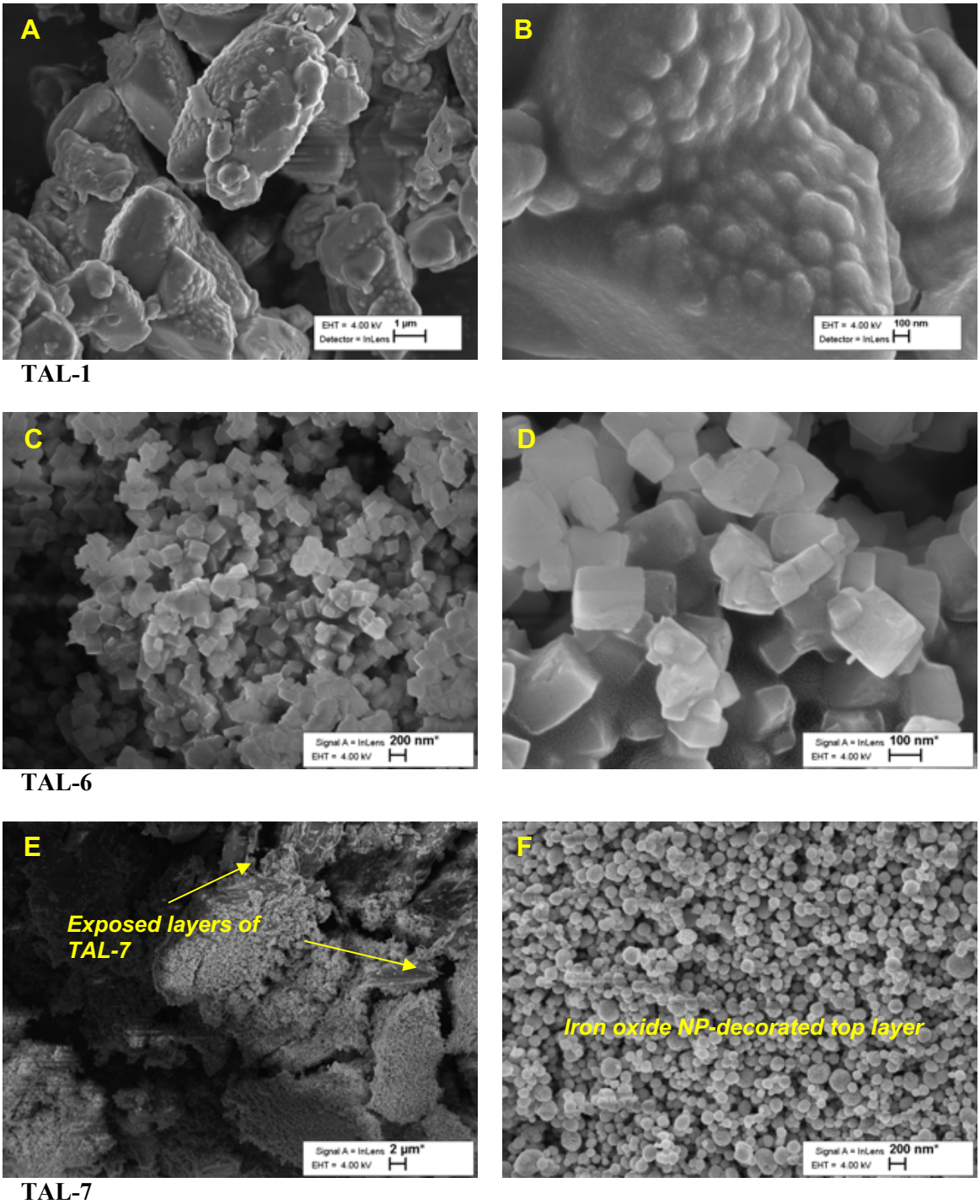

Figure S2. HRSEM images of TAL-1 (a,b), TAL-6 (c,d) and TAL-7 (e,f)

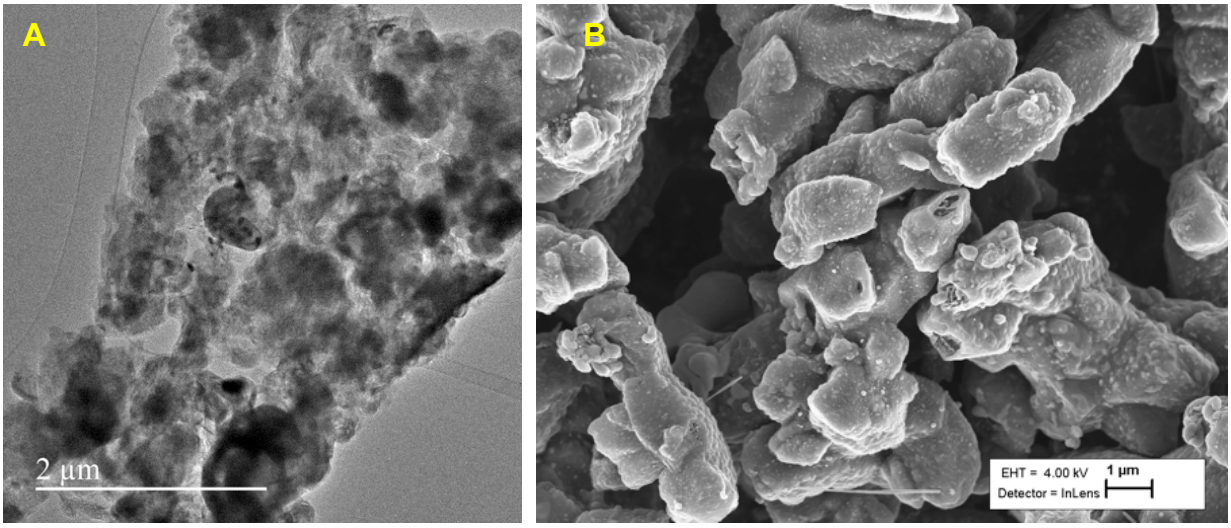

TAL-1-900

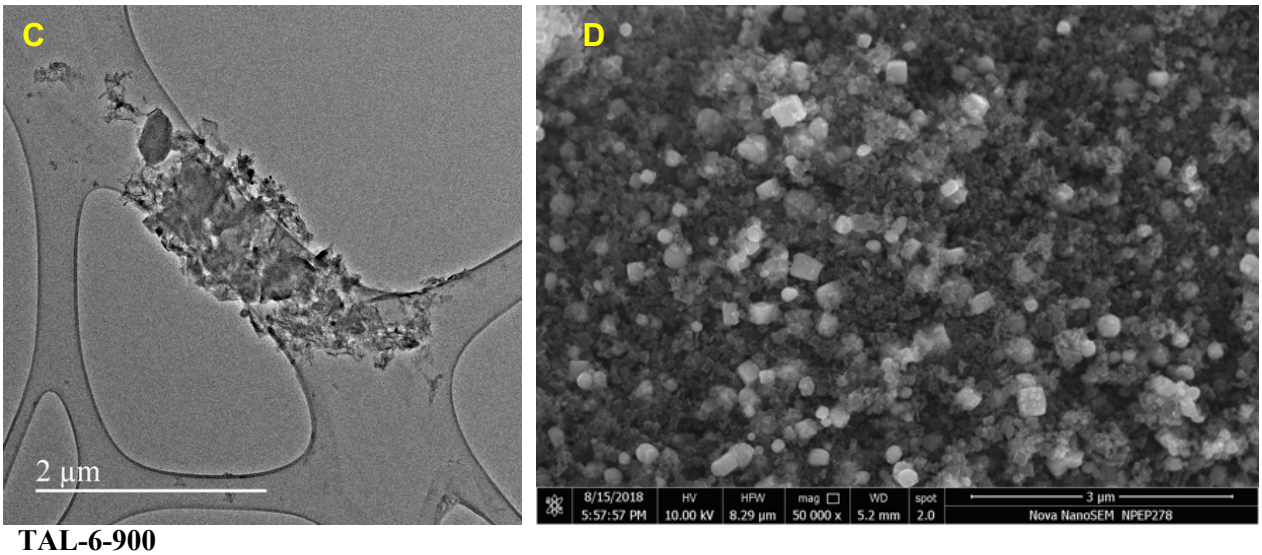

TAL-6-900

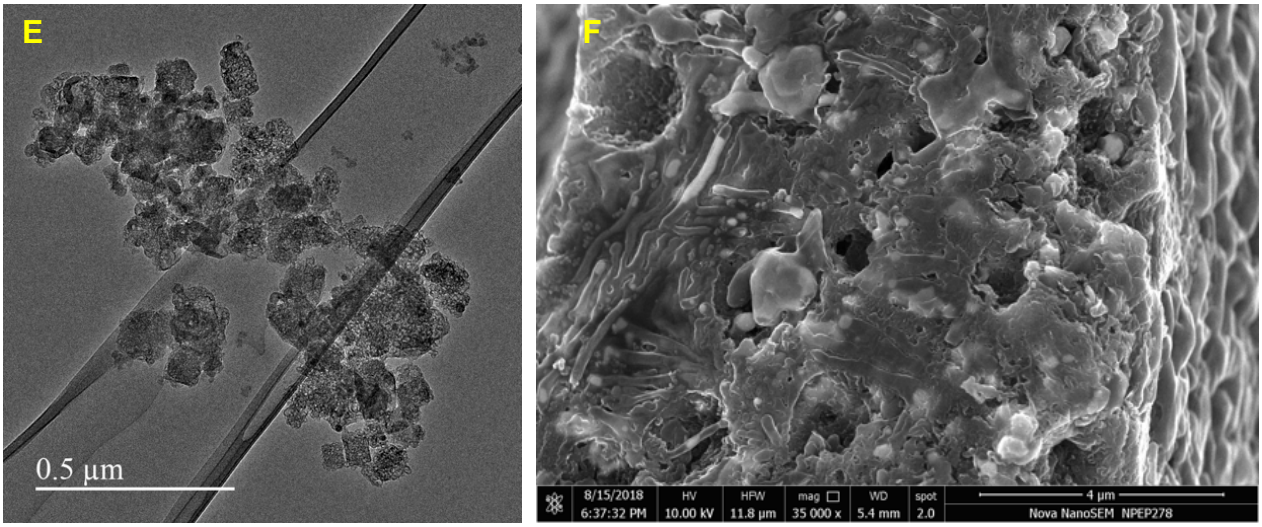

TAL-7-900

Figure S3. TEM and HRSEM images of TAL-1-900 (a,b), TAL-6-900 (c,d) and TAL-7-900 (e,f)

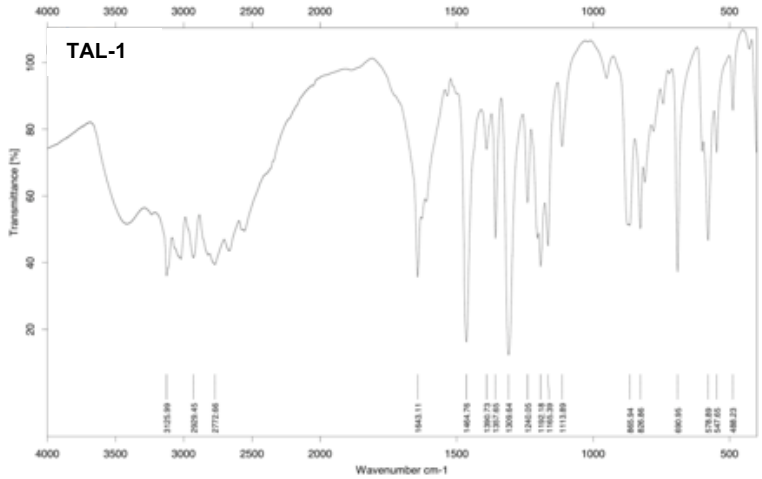

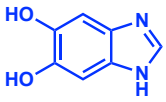

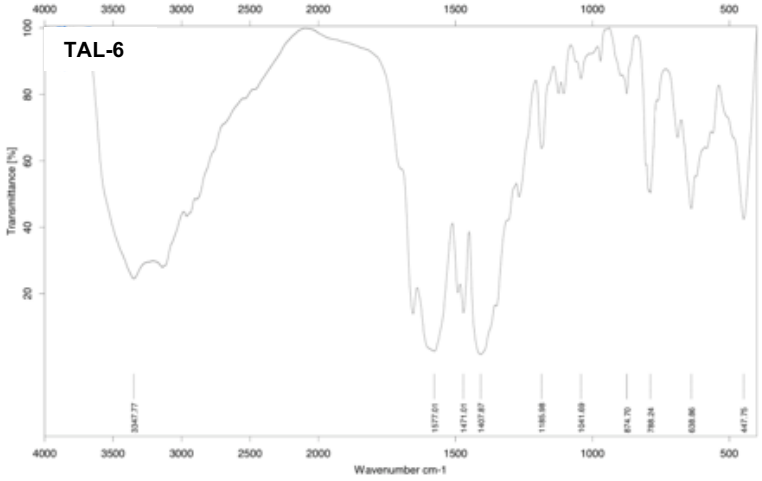

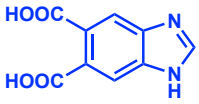

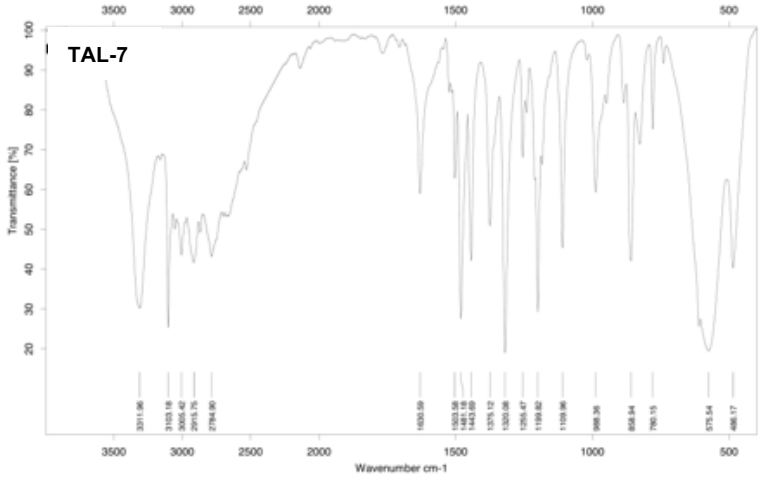

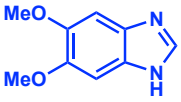

Figure S4. FTIR spectra of TAL-1, TAL-6 and TAL-7

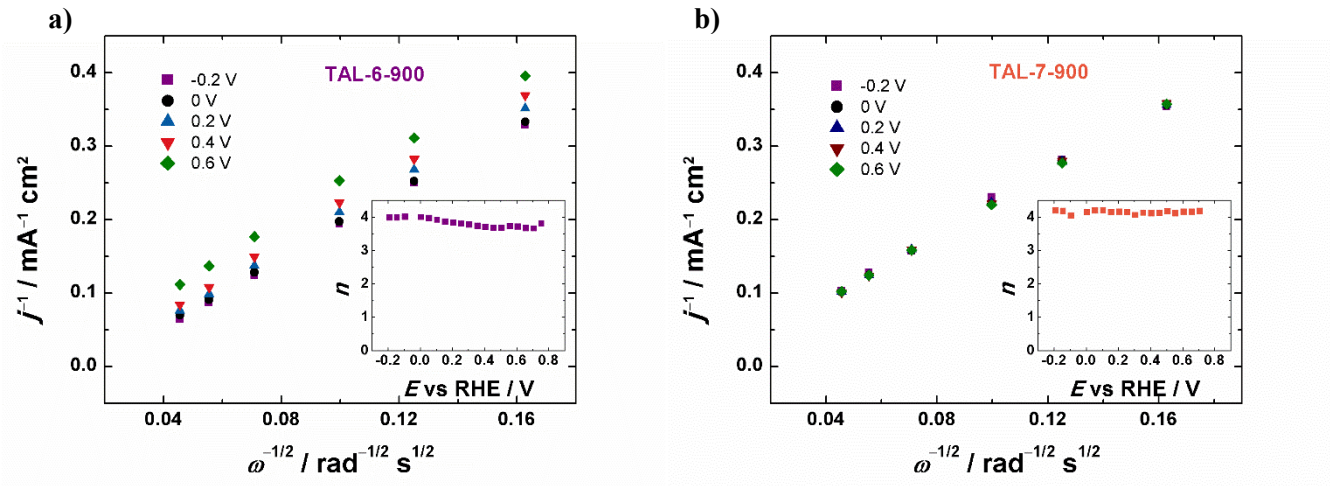

Figure S5. Koutecky–Levich plots for O_2 reduction on TAL-6-900 and TAL-7-900 modified GC electrodes; insets: number of electrons transferred per O_2 molecule

Table S3. Comparison of OER/ORR bifunctional activity ($\Delta E = E_{10}^{OER} – E_{1/2}^{ORR}$) for different catalysts measured in 0.1 M KOH [pyrolysis/graphitization was required in all instances]

catalyst	*precursors*	*ΔE*	*OER E_{10} @10mA cm^{-2}*	*ORR $E_{1/2}$ @−3 mA cm^{-2} @1600 rpm*	*reference/ DOI*
Mn/Fe-HIB-MOF	$Mn(NO_3)_2$ + $Fe(NO_3)_3$ + hexaminebenzene	0.63	1.51	0.88	*Energy Environ. Sci.* **2019,** *12,* ASAP. DOI:10.1039/c8ee02679g
NCMT-1000(3D)	facial cotton + $NH_3^{pyrolysis}$	0.63	1.52	0.89	*Energy Environ. Sci.* **2016,** *9,* 3079–3084. DOI:10.1039/c6ee02169g
N-GT(FeCoNi)-1000	DCDA + Fe, Co, Ni acetates	0.65	1.54	0.89	*Adv. Energy Mater.* **2016,** 6, 1601198. DOI:10.1002/aenm.201601198
CoNi@NCNT/NF	NF + melamine + $Co(NO_3)_2$	0.67	1.54	0.87	*Adv. Energy Mater.* **2018,** *8,* 1800480. DOI:10.1002/aenm.201800480
PNGF(op)	GO + $NH_4H_2PO_4$ + $(NH_4)_2HPO_4$ + cyanamide	0.705	1.55	0.845	*Energy Environ. Sci.* **2017,** *10,* 1186–1195. DOI:10.1039/c6ee03446b
TAL-1-900	***TAL-1, i.e. $FeCl_3$ + Ligand 1***	***0.73***	***1.60***	***0.87***	***This work***
NCNT-700	ZIF-67 + $H_2^{pyrolysis}$, i.e $Co(NO_3)_2$ + mim	0.73	1.60	0.87	*Nat. Energy* **2016,** *1,* 15006. DOI:10.1038/nenergy20156
Co_3O_4-C/NA	$Co(C_{12}H_6O_4)(H_2O)_4$ + Cu foil	0.74	1.52	0.78	*J. Am. Chem. Soc.* **2014,** *136,* 13295–13931. DOI:10.1021/ja5082553
Co_4N/CNW/CC	ZIF-67 + polypyrrole nanofibers + carbon cloths	0.74	1.54	0.80	*J. Am. Chem. Soc.* **2016,** *138,* 10226–10231. DOI:10.1021/jacs.6b05046
NiFe-LDH/ Fe–N–C (1:3)	$Ni_{0.78}Fe_{0.22}(OH)_x$/C + Fe-PANI	0.75	1.54	0.79	*Energy Environ. Sci.* **2016,** *9,* 2020–2024. DOI:10.1039/c6ee01046g
S,N-Fe/N/C-CNT	$FeCl_3$ + KSCN + CNT + bipy	0.75	1.60	0.85	*Angew. Chem. Int. Ed.* **2017,** *56,* 610–614. DOI:10.1002/anie.201610119
Fe/C/N-800	melamine + HCHO + Ketjenblack EC-300J + $Fe(NO_3)_3$	0.76	1.59	0.83	*J. Phys. Chem. C* **2015,** *119,* 2583–2588. DOI:10.1021/jp511515q
Fe/N/C-800	$Fe(OAc)_2$ + phen + PTCDA + BP2000 (carbon) + $NH_3^{pyrolysis}$	0.76	1.60	0.84	*Science* **2009,** *324,* 71–74. DOI:10.1126/science.1170051

Co_3O_4/N-rmGO	GO + $Co(OAc)_2$ + NH_3	0.77	1.60	0.83	*Nat. Mater.* **2011,** *10,* 780–786. DOI:10.1038/nmat3087
NCF-900	Ball milling $ZnCl_2$ with cicada sloughs	0.77	1.66	0.89	*J. Mater. A* **2018,** *6,* 7762–7769. DOI:10.1039/c8ta01078a
Fe_3C@NG800-0.2	urea + glucose + $Fe(NO_3)_3$+NGCM (denoted as NG800)	0.78	1.59	0.81	*ACS Appl. Mater. Inter.* **2015,** *7,* 21511–21520. DOI:10.1021/acsami.5b06708
Cu@NCNT/Co_xO_y	CNTs+CuNP (Cu@CNTs) cobalt oxide (Co_xO_y) NP	0.78	1.60	0.82	*Adv. Funct. Mater.* **2017,** *27,* 1605717. DOI:10.1002/adfm.201605717
TAL-7-900	***TAL-7, i.e. $FeCl_3$ + Ligand 3***	***0.78***	***1.61***	***0.83***	***This work***
Ni-MnO/rGO	PVA + GO + $Mn(OAc)_2$ + $Ni(OAc)_2$	0.82	1.60	0.78	*Adv. Mater.* **2018,** *30,* 1704609. DOI:10.1002/adma.201704609
N-GRW	melamine + cysteine	0.82	1.66	0.84	*Sci. Adv.* **2016,** *2,* e1501122. DOI:10.1126/sciadv.1501122
TAL-6-900	***TAL-6, i.e. $FeCl_3$ + Ligand 2***	***0.83***	***1.64***	***0.81***	***This work***
Pt/C (20 wt%)	control	0.87	1.73	0.86	This work
Pt/C (20 wt%)	control	0.90	1.76	0.86	*J. Phys. Chem. C* **2015,** *119,* 2583–2588. DOI:10.1021/jp511515q
IrO_2/C (20 wt%)	control	0.76	1.60	0.73	*J. Phys. Chem. C* **2015,** *119,* 2583–2588. DOI:10.1021/jp511515q

bipy = 2,2'-bipyridine; DCDA = dicyandiamide; GO = graphene oxide; LDH = layered double hydroxide; mim = *N*-methylimdazole; NCNT = *N*-doped carbon nanotubes; NCMT = *N*-doped carbon microtubes; NF = nickel foam; NG = nanocrystals on graphene; NGCM = *N*-doped graphene-like carbon materials; phen = 1,10-phenanthroline; PNGF = P,N-co-doped graphene frameworks; PTCDA = perylenetetracarboxylicdianhydride; PVA = poly(vinyl alcohol)

2 Methods

PXRD. The powder XRD pattern for TAL-1 were recorded on a Rigaku Ultima IV diffractometer with Cu Kα radiation (λ = 1.5406 Å, 40 kV at 40 mA) and using the silicon strip detector D/teX Ultra with the scan range of 2θ = 10.0–60.0°, scan step 0.02°, scan speed 5 deg/min. The powder XRD patterns for the rest incl. additional run for TAL-1 were recorded on a Bruker D8 Advanced diffractometer using Ni filtered Cu Kα radiation and LynxEye line detector. Scanning steps were 0.013° 2θ from 5° to 90 ° 2θ and total counting time was 173 s per step. The scan axes were $2\theta/\theta$. JCPDS Cards No. for α-Fe (#87-0722), Fe_3C (#89-2867), Fe_3O_4 (#75-0033), and α-Fe_2O_3 (#33-0664).

SEM. Surface morphology was studied by scanning electron microscopy (SEM) using Zeiss Ultra–55. The solid was deposited onto the carbon tape (TAL-1, TAL-6 and TAL-7 samples were covered with a thin gold layer to improve conductivity).

XPS. The surface elemental composition was investigated by X-ray photoelectron spectroscopy (XPS) using the Scienta SES-100 spectrometer. For preparing the samples, the catalytic materials were dispersed in isopropanol at a concentration of 2 mg mL^{-1} and deposited onto GC plates (1.1×1.1 cm). The samples were tested with a non-monochromatic twin anode X-ray tube (XR3E2), where the characteristic energies were 1253.6 eV (Mg $Ka_{1,2}$, FWHM 0.68 eV) and 1486.6 eV (Al $Ka_{1,2}$, FWHM 0.83 eV). The pressure in the analysis chamber was below 10^{-9} Torr and the source power was 300 W. Survey spectra were obtained using the following parameters: energy range 800 to 0 eV, pass energy 200 eV, step size 0.5 eV. High resolution XPS scans were performed using pass energy 200 eV and step size 0.1 eV. An Ag wire attached to the sample holders was used for energy reference (Ag $3_{d5/2}$ at 367.8 eV), no charging effects were observed. Peak fitting was done using CasaXPS (version 2.3.16) software.

TEM. Scanning transmission electron microscopy was done using FEI Titan 200 with 200 keV electron beam.

IR. Measured on Bruker Tensor 27 FT-IR using KBr pellets.

Electroanalytical studies. All electrochemical measurements, including ORR and OER tests were performed in a three-electrode glass cell, using a rotating disk electrode (RDE) setup and an Autolab potentiostat/galvanostat PGSTAT30 (Eco Chemie B.V.). A glassy carbon (GC) rod served as counter electrode. Potentials were measured against a reversible hydrogen electrode (RHE) connected to the cell through a Luggin capillary. GC disks (geometric area of 0.126 cm^2) polished to a mirror finish with 1 and 0.3 μm alumina slurries (Buehler) pressed into a Teflon holder served as working electrodes.

Prior to modification, the GC electrode was sonicated in both isopropanol and Milli-Q water for 5 min to remove polishing residues. The catalyst suspension was homogenized by sonication for 30 min and catalyst suspension was spin-coated onto the GC electrode and allowed to dry in air, yielding the catalyst loading of 800 μg cm^{-2}.

The electrolyte solution was prepared using Milli-Q water, KOH pellets (p.a. quality, Merck); saturated with pure O_2 (99.999%, AGA) and deaerated with Ar gas (99.999%, AGA). Comparison experiments were performed with 20 wt% Pt/C (E-TEK; loading of 20 μg_{Pt} cm^{-2}). The RDE technique was used to explore the electrocatalytic activity of the catalyst towards the ORR. Cyclic voltammograms were recorded at a potential sweep rate (v) of 50 mV s^{-1}. The RDE polarization curves were measured at different electrode rotation rates (ω): 360-4600 rpm. Electrode rotation rate was controlled using a CTV101 speed control unit connected to an EDI101 rotator (Radiometer). The background currents were recorded at 10 mV s^{-1} in argon-saturated 0.1 M KOH and were subtracted from the RDE data.

Koutecky−Levich (K–L) plots at various electrode potentials were constructed from the RDE data. The number of electrons transferred per O_2 molecule (n) was calculated from the RDE data using the K–L equation:

$$\frac{1}{j} = \frac{1}{j_k} + \frac{1}{j_d} = -\frac{1}{nFkC_{O_2}^b} - \frac{1}{0.62nFD_{O_2}^{2/3}v^{-1/6}C_{O_2}^b\omega^{1/2}}$$

where j denotes the measured current density at a specific potential, while j_k and j_d are the kinetic and diffusion-limited current densities, respectively. F denotes the Faraday constant (96,485 C mol^{-1}), k is the rate constant for electrochemical reduction of oxygen, $\boldsymbol{C_{O_2}^b}$ denotes the concentration of O_2 (1.2×10^{-6} mol cm^{-3} in 0.1 M KOH) while $\boldsymbol{D_{O_2}}$ represents the diffusion coefficient of O_2 (1.9×10^{-5} cm^2 s^{-1} in 0.1 M KOH), v is the kinematic viscosity of the solution (0.01 cm^2 s^{-1}) and ω is the rotation rate of the electrode (rad s^{-1}).

Accelerated durability tests were also performed by cycling electrodes 5000 times in the potential range between 0.6 and 1 V *vs.* RHE (ORR) and between 1.0 and 1.8 V *vs.* RHE (OER), using a scan rate of 100 mV s^{-1}. RDE polarization curves for ORR and OER were recorded before and after 5000 cycles and compared. The chronoamperometry measurements were conducted at the potential of 1.6 V vs. RHE and lasted for 10000 seconds in total. All experiments were carried out at room temperature (23 ± 1 °C).

3 Synthetic Procedures

General

All chemicals were used as supplied. Chromatographic separations were performed on ThoMar OHG silica gel 60Å (40–63 μm). Thin-layer chromatography was performed on Merck TLC Silica gel 60 F_{254} and visualized by UV (254 nm), $KMnO_4$ and/or phosphomolybdic acid. ^1H and ^{13}C NMR spectra were recorded on Bruker Avance 400 spectrometer. Residual solvent peaks were used as internal standards [1]. Chemical shifts are quoted in ppm using the following abbreviations: *s* singlet; *br* broad; or a combination thereof.

Preparation of Organic Linkers

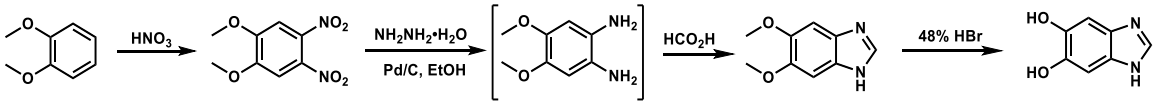

1,2-Dimethoxy-4,5-dinitrobenzene [2]
1,2-Dimethoxybenzene (11.08 g, 80.19 mmol, 1.0 equiv) was added dropwise into conc. HNO_3 (100 mL, 65%) at 0 °C, after addition, the mixture was left to stir at 80 °C. After 2 h, the mixture was cooled down to 0 °C, and the resulting precipitate was washed with distilled water until neutral to give the desired compound as a yellow needle crystal (15.39 g, 67.45 mmol, 84%).
^{1}H NMR (400 MHz, $CDCl_3$) δ 7.33 (s, 2H), 4.01 (s, 6H).
^{13}C NMR (100 MHz, $CDCl_3$) δ152.0, 136.8, 107.1, 57.2.

5,6-Dimethoxy-1*H*-benzo[*d*]imidazole [2]
Hydrazine monohydrate (22.6 mL, 464.7 mmol, 10.8 equiv) was added dropwise to a solution of 1,2-dimethoxy-4,5-dinitrobenzene (9.85 g, 43.2 mmol, 1.0 equiv) and Pd/C (10%, 0.985 g) in anhydrous EtOH (60 mL) at 0 °C, after addition, the mixture was left to stir at 80 °C. After 30 min, the mixture was filtered through silica gel (CAUTION! Pd/C on silica gel may catch fire!), concentrated under reduced pressure, to which formic acid (98%, 100 mL) was added, and the mixture was left to stir at 100 °C. After 16 h, the mixture was concentrated under reduced pressure, water (50 mL) added, and the solution was basified with solid K_2CO_3. The precipitate was collected, washed with water and dried to give the desired compound as a colorless solid (7.00 g, 39.3 mmol, 91%).
^{1}H NMR (400 MHz, DMSO-d_6) δ 8.03 (s, 1H), 7.14 (s, 2H), 3.82 (s, 6H).
^{13}C NMR (100 MHz, DMSO-d_6) δ 147.2, 141.1, 132.5, 99.2, 56.8.

1*H*-Benzo[*d*]imidazole-5,6-diol [2]
5,6-Dimethoxy-1*H*-benzo[*d*]imidazole (7.79 g, 43.7 mmol, 1.0 equiv) was added into HBr (48%, 50 mL), and the mixture was left to stir at 120 °C. After 4 h, the mixture was cooled down to 0 °C, and the precipitate was collected, washed with petroleum ether to give the desired compound as a colorless solid (4.59 g, 30.6 mmol, 70%).
^{1}H NMR (400 MHz, DMSO) δ 9.75 (s, 2H), 9.25 (s, 1H), 7.12 (s, 2H).
^{13}C NMR (100 MHz, DMSO) δ 146.4, 136.9, 123.7, 98.4.

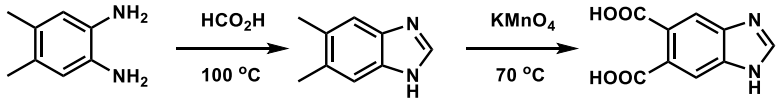

5,6-Dimethyl-1*H*-benzo[*d*]imidazole [3]
A solution of 4,5-dimethylbenzene-1,2-diamine (2.024 g, 14.860 mmol, 1.0 equiv) in formic acid (10 mL) was left to stir at 100 °C. After 4 h, the mixture was concentrated under reduced pressure, water added, the solution was basified with solid K_2CO_3, and the precipitate was collected, washed with water and dried to give the desired product as a colorless solid (1.813 g, 12.402 mmol, 83%).
^{1}H NMR (400 MHz, DMSO-d_6) δ 12.18 (br s, 1H), 8.05 (s, 1H), 7.34 (s, 2H), 2.30 (s, 6H).
^{13}C NMR (100 MHz, DMSO-d_6) δ 141.0, 130.1, 20.0, two carbons not observed.

1*H*-Benzo[*d*]imidazole-5,6-dicarboxylic acid [4]
A solution of $KMnO_4$ (19.594 g, 123.990 mmol, 10 equiv) was added dropwise into a solution of 5,6-dimethyl-1*H*-benzo[*d*]imidazole (1.813 g, 12.3990 mmol, 1.0 equiv) in water/*t*-BuOH (16 mL/16 mL), the mixture was left to stir gradually heating up to 70 °C. After addition, heating was turned off, the mixture was left to stir at RT for 15 min, after which Na_2SO_3 (4.765 g, 37.805 mmol, 3.0 equiv) was added, the mixture was then left to stir at 80 °C. After 30 min, the mixture was filtered through Celite, washed with boiling water, filtrate was concentrated under reduced pressure to approximately 50 mL, diluted with water, cooled down to 0 °C, acetic acid/water (18 mL/9 mL) added, precipitate was collected, dried to give the desired product as a colorless solid (711.2 mg, 3.4497 mmol, 28%).
^{1}H NMR (400 MHz, DMSO-d_6) δ 8.45 (s, 1H), 7.91 (s, 2H).
^{13}C NMR (100 MHz, DMSO-d_6) δ 169.1, 145.5, 127.5, 116.3, one carbon was not observed.

Preparation of TAL-1
$FeCl_3{\cdot}6H_2O$ (2.97 g, 10.99 mmol, 1.0 equiv) and 1*H*-benzo[*d*]imidazole-5,6-diol (3.30 g, 21.98 mmol, 2.0 equiv) was dissolved in a mixture of DMF (15 mL) and distilled water (15 mL), and the mixture was left to react at 100 °C. After 72 h, the mixture was cooled down to RT, centrifuged, washed with DMF (3×10 mL), and dried to give the desired material as a black solid (2.32 g).

Preparation of TAL-6
A solution of $FeCl_3 \cdot 6H_2O$ (440 mg, 1.629 mmol, 1.0 equiv) and 1*H*-benzo[*d*]imidazole-5,6-dicarboxylic acid (671 mg, 3.255 mmol, 2.0 equiv) in DMF/water (3 mL/3 mL) was left to stir at 100 °C. After 72 h, the mixture was cooled down to RT, centrifuged, the precipitate was washed with DMF (3×10 mL), and dried to give the desired material as a yellow solid (593 mg).

Preparation of TAL-7
A solution of $FeCl_3 \cdot 6H_2O$ (758 mg, 2.804 mmol, 1.0 equiv) and 5,6-dimethoxy-1*H*-benzo[*d*]imidazole (1.00 g, 5.610 mmol, 2.0 equiv) in DMF/water (3 mL/3 mL) was left to stir at 100 °C. After 72 h, the mixture was cooled down to RT, centrifuged, the precipitate was washed with DMF (3×10 mL), and dried to give the desired material as a red solid (599 mg).

Carbonization
Carbonization was undertaken at 900 °C (N_2, rapid heat, 2 h, slow cooling). Carbonized materials were suspended in a 1:1 mixture of 0.5 M H_2SO_4 and 0.5 M HNO_3, stirred for 8 h at 50 °C, filtered, and re-carbonized under N_2 at 900 °C for 2 h to give the acid leached materials **TAL-1-900**, **TAL-6-900** and **TAL-7-900**.

4 References

1. Gottlieb, H. E., Kotlyar, V. & Nudelman, A. NMR chemical shifts of common laboratory solvents as trace impurities. *J. Org. Chem.* **1997,** *62,* 7512–7515. doi:10.1021/jo971176v
2. Fan, K. W., Peterson, M. B., Ellersdorfer, P. & Granville, A. M. Expanding the aqueous-based redox-facilitated self-polymerization chemistry of catecholamines to 5,6-dihydroxy-1*H*-benzimidazole and its 2-substituted derivatives. *RSC Adv.* **2016,** *6,* 25203–25214. doi:10.1039/c5ra25590b
3. Karuvalam, R. P.; Siji, M.; Divia, N.; Haridas, K. R. Tetra butyl ammonium chloride catalyzed synthesis of substituted benzimidazoles under microwave conditions. *J. Kor. Chem. Soc.* **2010,** *54,* 589–593. doi:10.5012/jkcs.2010.54.5.589
4. Leonard, N. J.; Kazmierczak, F. A convenient synthesis of lin-benzopurines through a common intermediate. *J. Org. Chem.* **1987,** *52,* 2933–2935. doi:10.1021/jo00389a055

5 NMR Spectra

1,2-Dimethoxy-4,5-dinitrobenzene

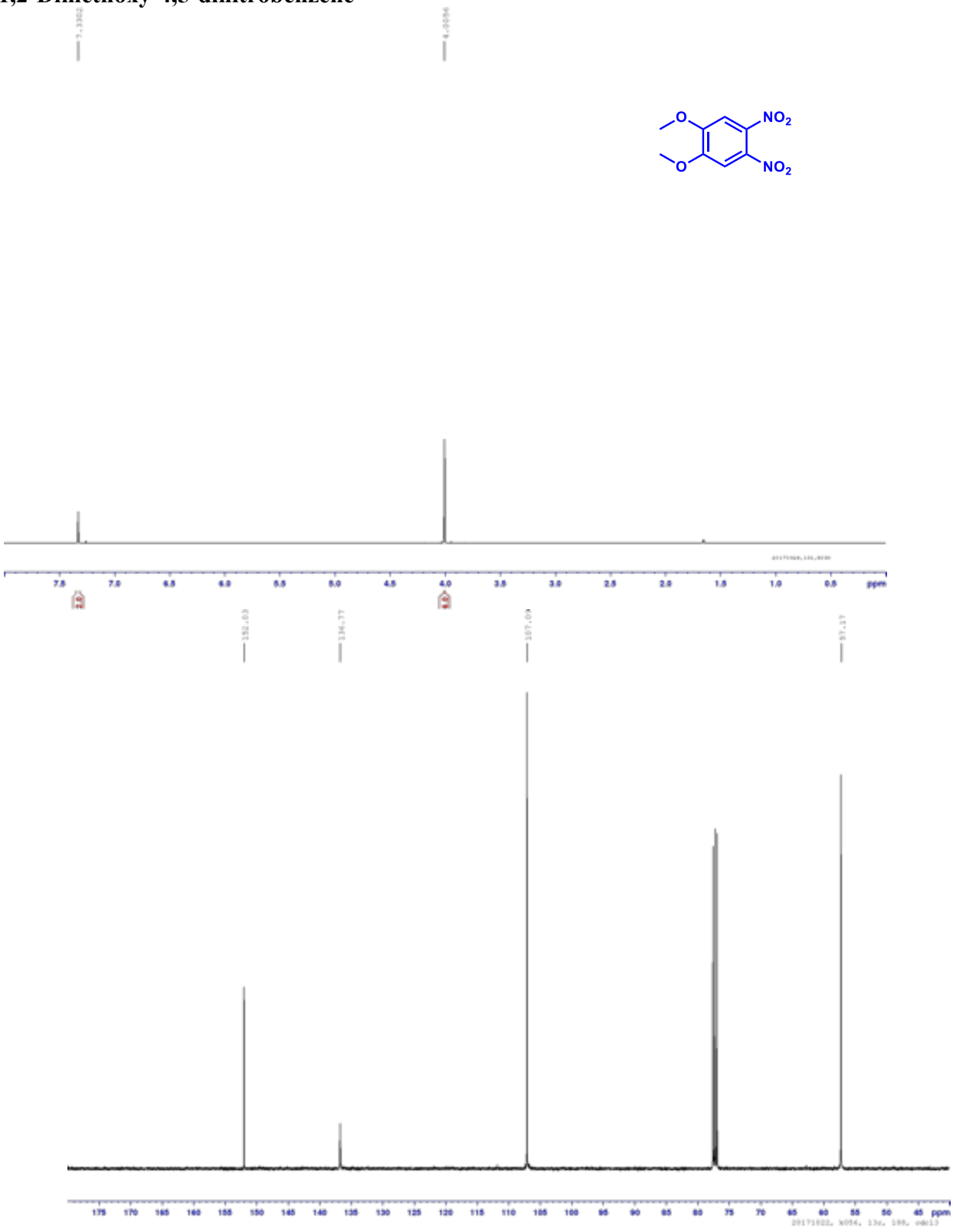

5,6-Dimethoxy-1*H*-benzo[*d*]imidazole

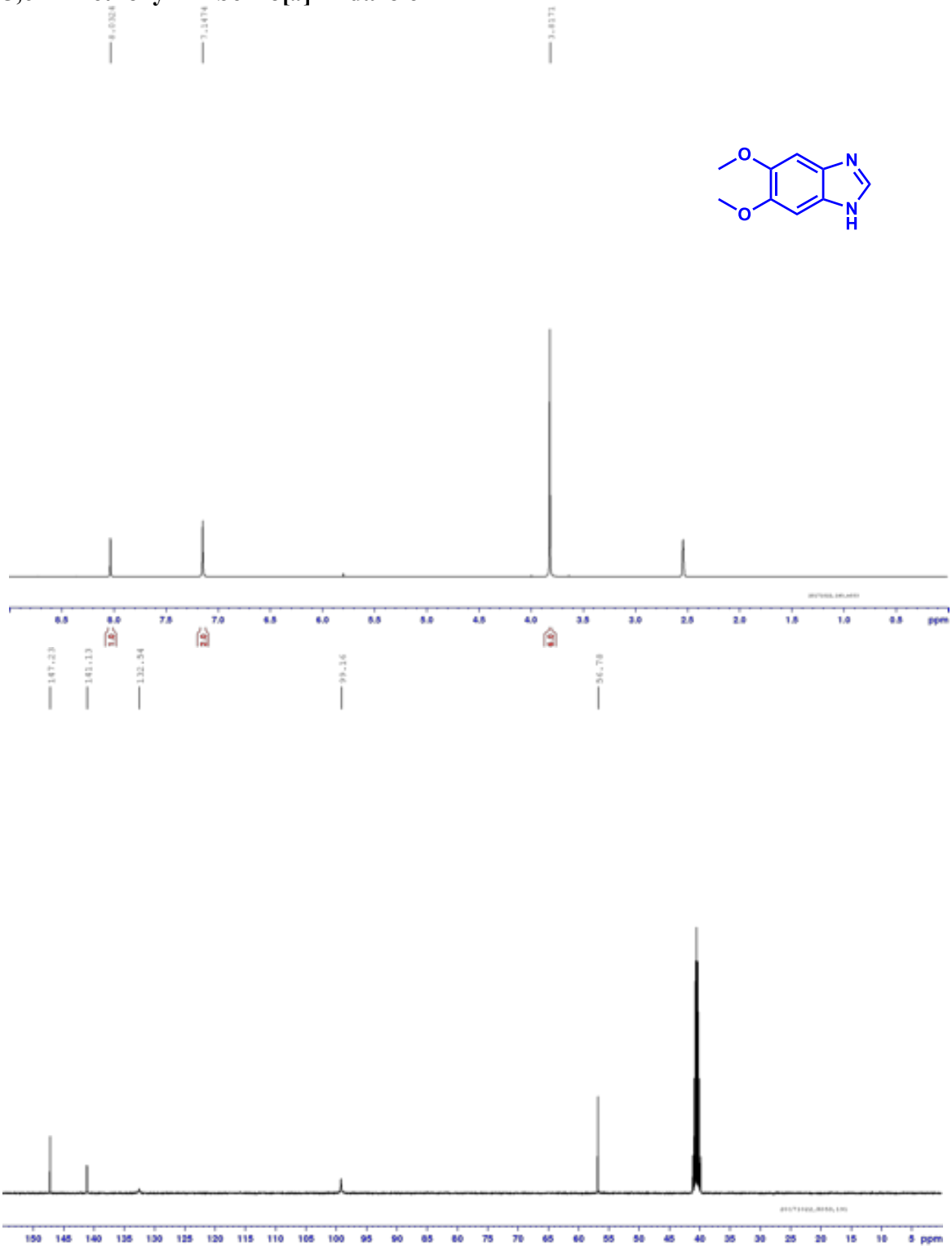

1*H*-Benzo[*d*]imidazole-5,6-diol

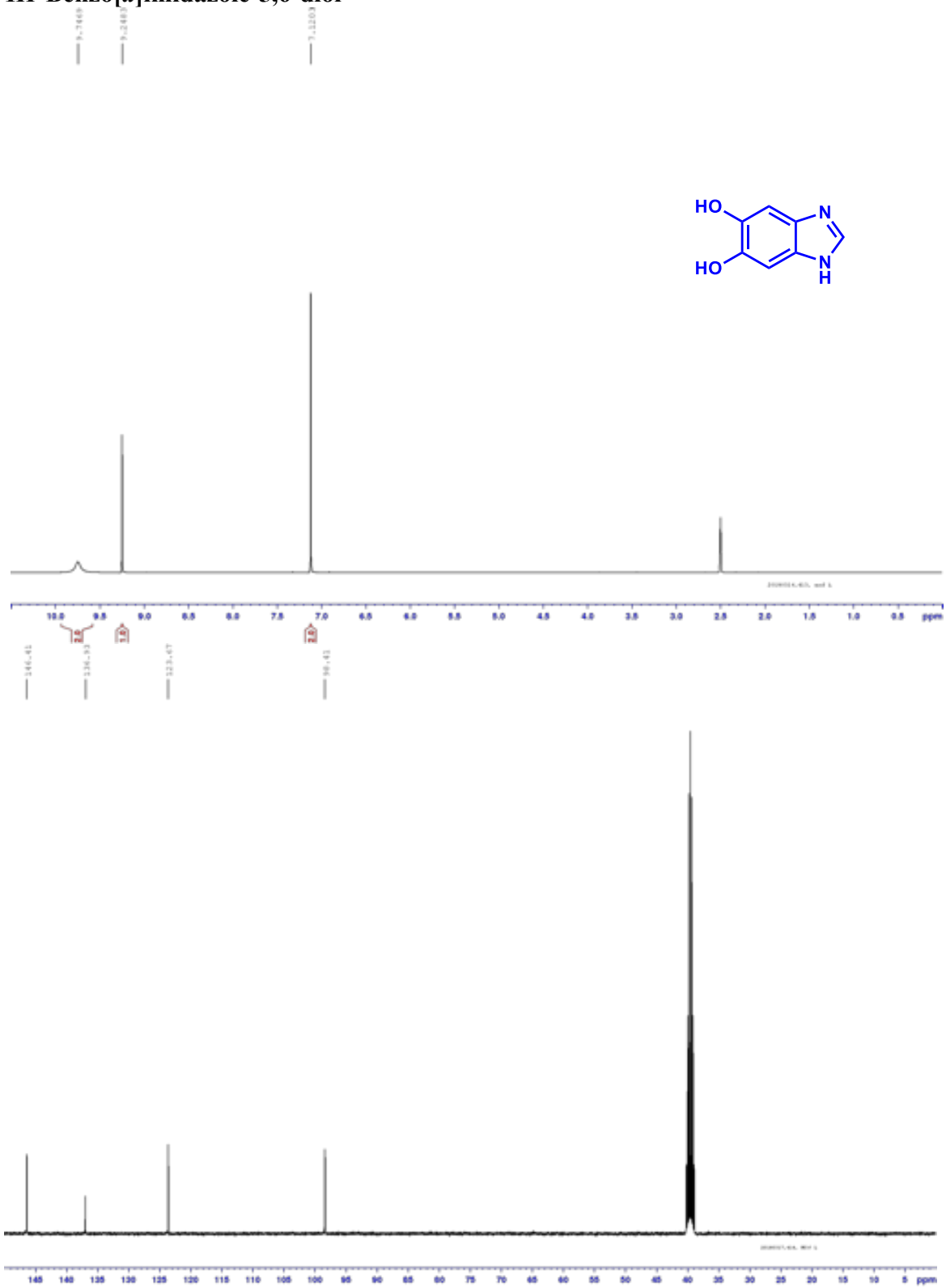

5,6-Dimethyl-1*H*-benzo[*d*]imidazole

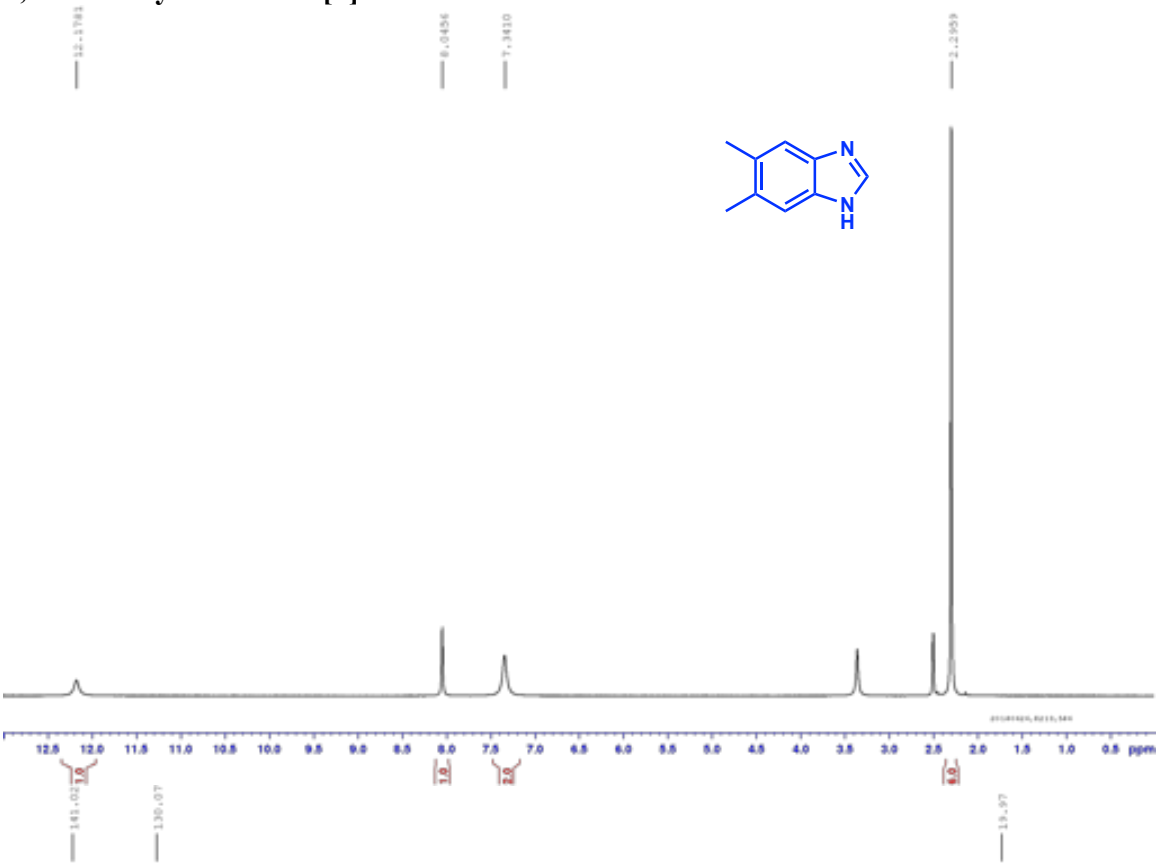

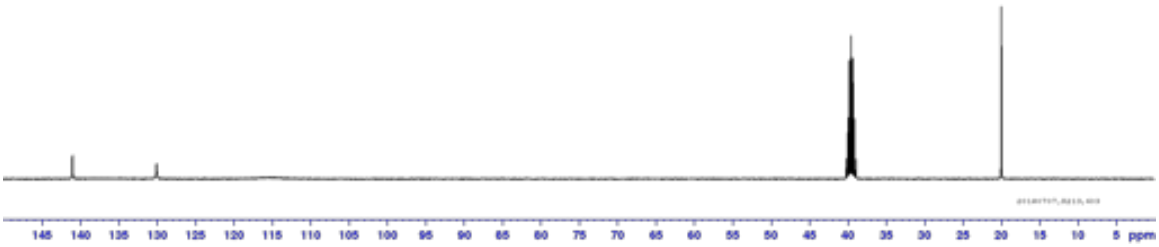

1*H*-Benzo[*d*]imidazole-5,6-dicarboxylic acid